Research Article | Vol. 25, No. 25 | 11 Dec 2017 | OPTICS EXPRESS 31077
Optics EXPRESS

Material anisotropy as a degree of freedom in optical design

OMER TZANG,* ANURAG AGRAWAL, AND RAFAEL PIESTUN

Department of Electrical, Computer, and Energy Engineering, University of Colorado, Boulder, CO 80309, USA
**omer.tzang@colorado.edu*

Abstract: We present an approach for the design of refractive optical elements using materials degrees of freedom that are accessible via engineered materials. Starting from first principles and an unconstrained general material, we specify homogeneous refractive lenses that focus light with diffraction-limited resolution resulting from a tailored anisotropic refractive index. We analyze the performance, physical feasibility, and advantages over isotropic lenses. Materials degrees of freedom enable new flexibility for imaging system designs with lower complexity expanding the existing aspheric and graded index paradigms.

OCIS codes: (080.3630) Lenses; (160.1190) Anisotropic optical materials; (220.2740) Geometric optical design.

References and links

1. M. Born and E. Wolf, *Principles of Optics: Electromagnetic Theory of Propagation, Interference and Diffraction of Light* (Elsevier, 1980).
2. V. N. Mahajan, *Optical Imaging and Aberrations: Part I. Ray Geometrical Optics (SPIE Press Monograph Vol. PM45)* (SPIE Publications, 1998).
3. R. Kingslake and R. B. Johnson, *Lens Design Fundamentals*, 2nd ed. (SPIE Press, 2010).
4. D. G. and W. K. A. B. Shorey, "Surface Finishing of Complex Optics," Opt. Photon. News **18**, 14–16 (2007).
5. V. Nguyen, S. Larouche, N. Landy, J. S. Lee, and D. R. Smith, "Quantitative comparison of gradient index and refractive lenses," J. Opt. Soc. Am. A **29**(11), 2479–2497 (2012).
6. H.-P. Herzig, *Micro-Optics: Elements, Systems And Applications* (CRC Press, 1997).
7. G. Beadie, J. S. Shirk, A. Rosenberg, P. A. Lane, E. Fleet, A. R. Kamdar, Y. Jin, M. Ponting, T. Kazmierczak, Y. Yang, A. Hiltner, and E. Baer, "Optical properties of a bio-inspired gradient refractive index polymer lens," Opt. Express **16**(15), 11540–11547 (2008).
8. C. Weber, C. G. Dupuy, J. P. Harmon, and D. M. Schut, "Inks for 3d printing gradient refractive index (grin) optical components," U.S. patent US Patent App. 15/240,263 (2017).
9. F. Z. Fang, X. D. Zhang, A. Weckenmann, G. X. Zhang, and C. Evans, "Manufacturing and measurement of freeform optics," CIRP Ann. - Manuf. Technol. **62**, 823–846 (2013).
10. K. P. Thompson and J. P. Rolland, "Freeform optical surfaces: a Revolution in imaging optical design," Opt. Photonics News, Optical Soc. Am. **32**, 30–35 (2012).
11. P. Lalanne and P. Chavel, "Metalenses at visible wavelengths: past, present, perspectives," Laser Photonics Rev. **11**, 101130F (2017).
12. P. Lalanne, S. Astilean, P. Chavel, E. Cambril, and H. Launois, "Design and fabrication of blazed binary diffractive elements with sampling periods smaller than the structural cutoff," J. Opt. Soc. Am. A **16**, 1143 (1999).
13. D. D. Holm, *Geometric Mechanics, Part I: Dynamics and Symmetry* (Imperial College, 2008).
14. S. C. McClain, L. W. Hillman, and R. a. Chipman, "Polarization ray tracing in anisotropic optically active media. II. Theory and physics," J. Opt. Soc. Am. A **10**, 2383 (1993).
15. A. J. Hoffman, L. Alekseyev, S. S. Howard, K. J. Franz, D. Wasserman, V. A. Podolskiy, E. E. Narimanov, D. L. Sivco, and C. Gmachl, "Negative refraction in semiconductor metamaterials," Nat. Mater. **6**(12), 946–950 (2007).
16. J. S. T. Smalley, F. Vallini, S. A. Montoya, L. Ferrari, S. Shahin, C. T. Riley, B. Kanté, E. E. Fullerton, Z. Liu, and Y. Fainman, "Luminescent hyperbolic metasurfaces," Nat. Commun. **8**, 13793 (2017).
17. L. Ferrari, J. S. T. Smalley, Y. Fainman, and Z. Liu, "Hyperbolic metamaterials for dispersion-assisted directional light emission," Nanoscale **9**(26), 9034–9048 (2017).
18. J. Liu, R. Mendis, and D. M. Mittleman, "A Maxwell's fish eye lens for the terahertz region," Appl. Phys. Lett. **103**, 031104 (2013).
19. R. Mendis, A. Nag, F. Chen, and D. M. Mittleman, "A tunable universal terahertz filter using artificial dielectrics based on parallel-plate waveguides," Appl. Phys. Lett. **97**, 1–4 (2010).
20. R. Mendis, M. Nagai, Y. Wang, N. Karl, and D. M. Mittleman, "THz artificial dielectric lens," Sci. Rep. **6**, 1–8 (2016).

#303878 https://doi.org/10.1364/OE.25.031077
Journal © 2017 Received 2 Aug 2017; revised 9 Oct 2017; accepted 9 Oct 2017; published 29 Nov 2017

Optics EXPRESS

21. C. T. Riley, J. S. T. Smalley, K. W. Post, D. N. Basov, Y. Fainman, D. Wang, Z. Liu, and D. J. Sirbuly, "High-Quality, Ultraconformal Aluminum-Doped Zinc Oxide Nanoplasmonic and Hyperbolic Metamaterials," Small **12**(7), 892–901 (2016).
22. M. S. Rill, C. Plet, M. Thiel, I. Staude, G. von Freymann, S. Linden, and M. Wegener, "Photonic metamaterials by direct laser writing and silver chemical vapour deposition," Nat. Mater. **7**(7), 543–546 (2008).
23. U. Levy, M. Abashin, K. Ikeda, A. Krishnamoorthy, J. Cunningham, and Y. Fainman, "Inhomogenous dielectric metamaterials with space-variant polarizability," Phys. Rev. Lett. **98**(24), 243901 (2007).
24. Z. A. Sechrist, B. T. Schwartz, J. H. Lee, J. A. McCormick, R. Piestun, W. Park, and S. M. George, "Modification of Opal Photonic Crystals Using Al2O3 Atomic Layer Deposition," Chem. Mater. **18**, 3562–3570 (2006).
25. W. Cai, T. J. Reber, and R. Piestun, "Computer-generated volume holograms fabricated by femtosecond laser micromachining," Opt. Lett. **31**(12), 1836–1838 (2006).
26. E. N. Glezer, M. Milosavljevic, L. Huang, R. J. Finlay, T.-H. Her, J. P. Callan, and E. Mazur, "Three-dimensional optical storage inside transparent materials," Opt. Lett. **21**(24), 2023–2025 (1996).
27. S. Kawata, H. B. Sun, T. Tanaka, and K. Takada, "Finer features for functional microdevices," Nature **412**(6848), 697–698 (2001).
28. T. D. Gerke and R. Piestun, "Aperiodic computer-generated volume holograms improve the performance of amplitude volume gratings," Opt. Express **15**(23), 14954–14960 (2007).
29. W. Cai, A. R. Libertun, and R. Piestun, "Polarization selective computer-generated holograms realized in glass by femtosecond laser induced nanogratings," Opt. Express **14**(9), 3785–3791 (2006).

1. Introduction

Classical optical imaging systems consist of a series of refracting (or reflecting) surfaces interfacing among homogeneous isotropic materials that generally have a common axis of rotational symmetry. The surfaces are used to bend light rays originating from an object following the laws of geometrical optics to form an image. Fundamental considerations show that perfect imaging is possible in principle, but only with unit magnification [1]. According to the Gaussian optics approximation of small angles [2], the law of refraction takes a simple (linear) form. In this paraxial approximation, all the rays diverging from a point object and propagating through the system converge to a point named the Gaussian image point. However, beyond this approximation, rays are traced according to the exact geometrical optics laws and they generally do not converge to a point, resulting in aberrations.

Traditional optical design aims at minimizing such aberrations via multiple surface and/or multiple material systems that meet a set of performance requirements and constraints [2]. Modern lens design can also take advantage of aspheric [3,4], gradient index [5], diffractive, or holographic lenses [6] to reduce aberrations and overall complexity and size. In effect, current approaches to isomorphic imaging take advantage of various freedoms to improve lens performance: Graded-index optics exploits the flexibility of slowly varying inhomogeneities [5,7,8], aspheric [2,3] and freeform optics [9,10] exploit departures of surfaces from sphericity, while diffractive lenses [6] take advantage of diffraction effects, possibly including metamaterials to enhance performance [11,12]. However, even with all these techniques at hand, optical systems often have significant complexity in the form of multiple elements, unwieldy form factor, size, and weight.

In this work, we present a different and complementary approach for the design of refractive optical elements based on anisotropy, taking advantage of materials degrees of freedom without any a priori assumption on their physical properties. The materials characteristics are determined, based on first principles, to control the refraction angles while targeting a specific imaging task. In particular, we derive the required index anisotropy prescription for perfect focusing using a cylindrical homogeneous singlet. We show that, in principle, the resulting material specifications are accessible via artificial dielectrics and metamaterials. We explore the fundamental and practical limitations for implementation of this paradigm as well as application opportunities.

This paper is organized as follows: In section 2 we present the mathematical and physical concepts defining tailored anisotropic refractive index optics. In section 3 we present design studies of plano-convex and bi-convex lenses, while section 4 discusses optical materials for

Optics EXPRESS

implementing the design. Several appendices expand the topics presented in the prior sections.

2. Specification of homogeneous material index *n(θ)* for optimal focusing

The design principle for tailored refraction via anisotropic materials (TRAM) seeks to specify an anisotropic homogenous material with refractive index $n(\theta)$, where θ is the direction of rays, such that the target imaging properties are optimal. We calculate $n(\theta)$ for the desired optical response of the system to each incoming ray, effectively steering the rays to the desired focal point. While such geometric construction is always possible for a pair of conjugate points, to be physically meaningful, all resulting rays must satisfy Fermat's principle. Therefore, the process involves solving for a material that produces a stationary point following general anisotropic ray tracing principles. While the direct problem of ray tracing given a geometry and material is well understood, the material inverse problem proposed here has not been tackled before. We therefore start by stating the fundamental TRAM inverse problem as follows:

Given a lens geometry find the material anisotropic index n(θ) such that an optical performance quality metric is optimized, subject to anisotropic ray tracing rules including Fermat's principle.

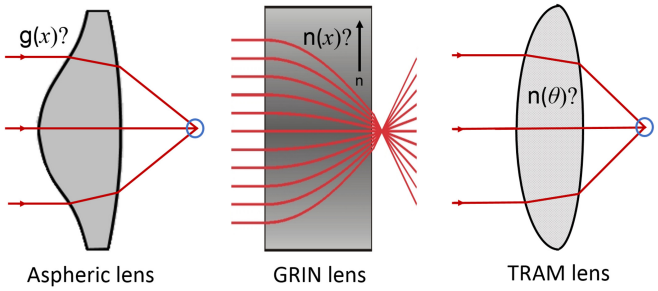

Fig. 1. Principle of tailored refraction via anisotropic materials (TRAM) design. Aspheric and GRIN lens approaches are depicted for comparison. $g(x)$ is the surface shape of the aspheric or freeform lens, $n(x)$ is an arbitrary refractive index profile, and $n(\theta)$ is the anisotropic refractive index described by an index that depends on the direction of propagation. For perfect focusing, we calculate the angle dependent refractive index that tunes the refraction angle at various positions of the interface.

Here we focus on tailoring the material for a given geometry, e.g. a lens with given curvature and width. However, the process can be extended to the joint optimization of the geometry and material, such as radii of curvature, width, asphericity, multi-elements, etc. This process is not different from conventional optical design, with the key innovation offered by the flexibility to tailor the material anisotropy for a specific task. Pure TRAM design is different from aspheric and freeform design in that the material properties rather than the surface relief is optimized. As opposed to GRIN, in which the refractive index varies across the material, pure TRAM design utilizes homogenous materials with anisotropic properties. These differences are illustrated in Fig. 1. Notwithstanding, TRAM is ultimately not meant to compete with the other design approaches but rather complement and enhance them.

TRAM ray tracing

At the interface of air and a TRAM material, ray tracing follows the rules of anisotropic refraction. Accordingly, a ray follows the direction of the Poynting vector $\hat{s}$ (the direction of energy flux of the electromagnetic field), which is normal to the index surface and conserves transverse momentum. Characteristically, the iso-phase surfaces are normal to the $\hat{k}$-vector, as depicted in Fig. 2. The angle α between the $\hat{k}$-vector and the Poynting vector is given by

Optics EXPRESS

$\tan\alpha = -dn_z/dn_x$ (see Fig. 2(a) and Appendix A); where n_x and n_z are the components of the index surface. Furthermore,

$$\tan\alpha = \frac{1}{n}\frac{dn}{d\theta} \tag{1}$$

where $dn/d\theta$ is the gradient to the index surface at the refractive point (See Appendix A).

Fermat's principle and optical path length

Fermat's principle establishes that the optical path length that light travels between the two points is stationary [13]. In order for the specified material to be physically meaningful (i.e. consistent with a given set of ray trajectories), rays have to follow this basic principle. The design process thus imposes a stationary optical path difference. We recall that the optical path length in anisotropic media is calculated by the projection of the $\hat{k}$-vector along the ray path multiplied by the respective refractive index: OPL = $nl_i\hat{k}\cdot\hat{s}$, as illustrated in Fig. 2(c) [14].

As part of the design of an anisotropic lens, we calculate the optical path lengths of all rays and keep the optical path length stationary by imposing that the maximum of the path difference among any two rays is zero. The result is the selection of refractive index profiles that satisfy Fermat's principle. This step is a physical validation of the design as illustrated in more detail in Fig. 3(d) and Appendix B. In this paper we consider perfect focusing in the geometrical optics sense, namely a diffraction limited spot size. We consider optimization for on axis foci and assume monochromatic light (or no chromatic dispersion).

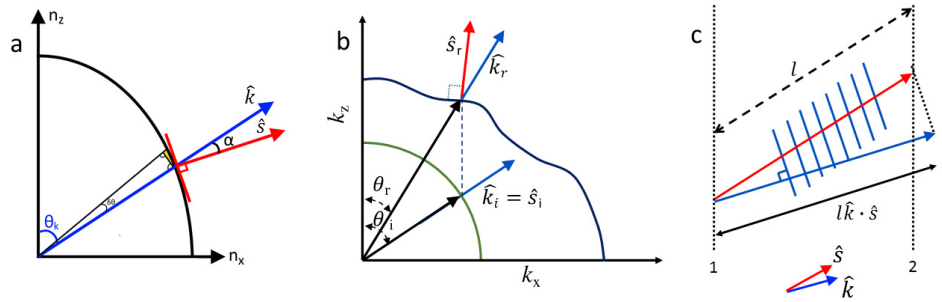

Fig. 2. Rays, wavefronts, refraction and optical path length in TRAM. (a) The direction of the ray $(\hat{s})$ is along the normal to the index surface at a given point, which is typically different from the direction of the $\hat{k}$-vector. n_x and n_z are the components of the index surface. (b) Schematic of the relationship between angle of incidence and angle of refraction when transitioning between isotropic (ex: air) and a TRAM (anisotropic) material with a generic $\hat{k}$-surface relationship. The dotted lines represent conservation of transverse momentum. (c) The optical path length is determined by the projection of the ray in the k direction and the index of refraction: OPL = $nl_i\hat{k}\cdot\hat{s}$.

Focusing by a single cylindrical interface

In order to illustrate the procedure, we first describe perfect focusing with a single cylindrical interface. The geometry is depicted in Fig. 3(a), where rays parallel to the optical axis (i.e. object at infinity) are refracted at the cylindrical interface. R is the radius of curvature and s_i is the distance between the desired image and the interface in the direction parallel to the rays. θ_k and θ_s are respectively the angle of the $\hat{k}$-vector and the angle of the refracted ray with the direction of incoming rays. The ideal design should focus all parallel rays to one point, at distance s_i. We start by defining the Poynting vector angle as follows:

Optics EXPRESS

$$\theta_s = \theta_k - \alpha = \theta_k - \tan^{-1}\left(\frac{1}{n}\frac{dn}{d\theta_k}\right), \tag{2}$$

$$\frac{dn}{d\theta_k} = n\tan\left(\theta_k - \theta_{s_{ideal}}\right) \tag{3}$$

This is a first order linear ordinary differential equation (ODE) with the initial condition of $n_{\theta=0} = 1.5$ (or any other value for the index of the ray that is incident normal to the interface). Note that the angle $\theta_{s_{ideal}}$ in Fig. 3(a) can be calculated trigonometrically for each angle ϕ. Therefore, for tailored focusing of the Poynting vector to distance s_i, we can simply define the ideal $\theta_{s_{ideal}}$ as a function of the geometry (ϕ).

$$\theta_{s_{ideal}} = \tan^{-1}\left(\frac{R\sin\phi}{s_i - R(1-\cos\phi)}\right) \tag{4}$$

We now combine Eqs. (2) and (3) and formulate an ODE that represents the ideal focusing as a function of $n(\theta)$ and θ_k, considering the anisotropic refraction rules

$$\frac{dn}{d\theta_k} = n\tan\left(\theta_k - \tan^{-1}\left(\frac{R\sin\phi}{s_i - R(1-\cos\phi)}\right)\right) \tag{5}$$

where $n_{\theta=0} = 1.5$ is the initial condition, and $\phi = \tan^{-1}\left(n\sin\theta_k / \left(n\cos\theta_k - 1\right)\right)$ is a trigonometric relation of angles at the point of refraction. Using Snell's law, $\sin\phi = n\sin(\theta_2) = n\sin(\phi - \theta_k)$, where θ_2 is defined in Fig. 3(a), Eq. (4) provides solutions for the index $n(\theta_k)$ that generate a perfect focus. The equation has the form $dn/d\theta_k = f(n,\theta_k)$, with $n_{\theta=0}$ as an initial condition, and can be solved numerically.

The resulting $n(\theta_k)$ for a spherical surface with R = 1, object at infinity, and focusing to s_i = 3 (the paraxial value expected for an isotropic material of index 1.5) is shown in Fig. 3.

Figure 3(b) presents the ray tracing (red) for the designed anisotropic material, showing ideal focusing. We also plot the $\hat{k}$-vector directions to illustrate the fact that they can be quite different, contrary to the situation in isotropic media. Here the $\hat{k}$-vectors do not converge to a point while the rays do. In order to be physically meaningful, rays have to follow Fermat's principle. The design process thus imposes a stationary optical path difference. Hence, we calculate the optical path difference (OPD) for varying s_i to find a solution that satisfies Fermat's principle, namely OPD = 0, for all its rays. This is exemplified in Fig. 3(d), showing a plot of the maximal OPD as the focal point is shifted around s_i = 3 (the isotropic paraxial solution).

Optics EXPRESS

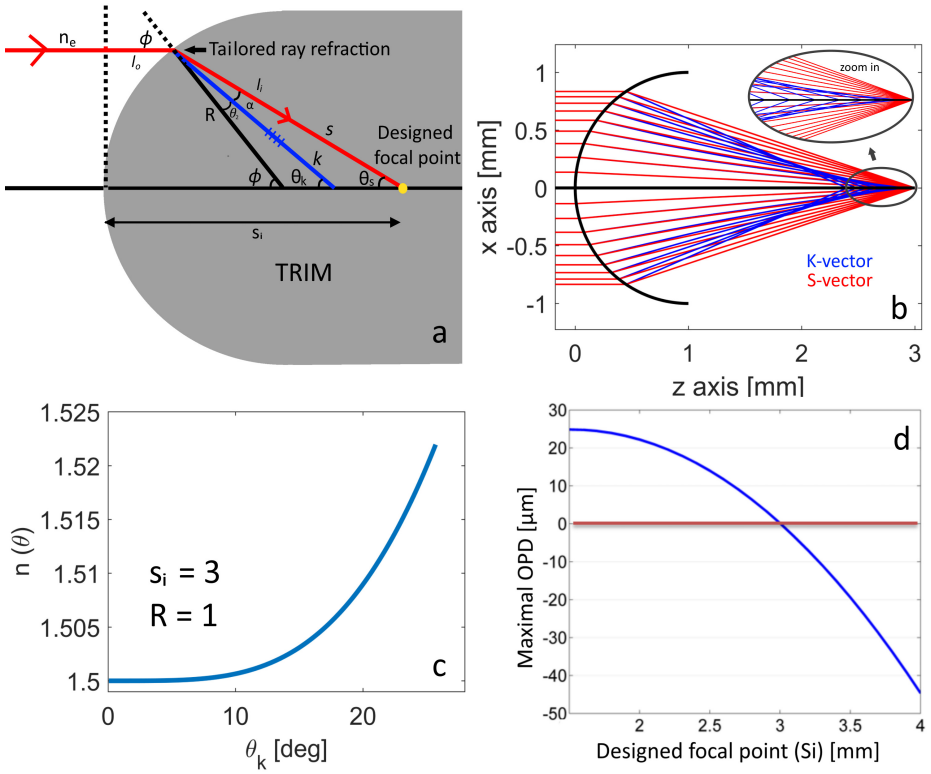

Fig. 3. Focusing through a cylindrical interface. (a) Refraction of a ray at a cylindrical TRAM interface. The rays (red) refract in the direction of the Poynting vector $\hat{s}$ whereas the phase fronts propagate in the direction of the $\hat{k}$-vector (blue). (b) Ray tracing (red) showing ideal focusing for the anisotropic material described in (a) and the wave vector directions (blue) for reference. Zoom in on the Ray tracing showed in the top right inset. (c) Optimized $n(\theta)$ curve for the case of single spherical interface, $s_i = 3$, $R = 1$, object at infinity. (d) Fermat principle constraint – for each focal location s_i, a $n(\theta)$ curve is generated, ray tracing performed, and the OPD calculated. The blue curve shows the calculated OPD for each focal length. The red curve is OPD = 0. The crossing of the blue and red curves represents the solutions satisfying Fermat principle. The found solution is very close to the paraxial isotropic solution $s_i = 3.005$, and the deviation due to numerical accuracy.

3. Design studies

Cylindrical plano-convex lens

Let us consider next a plano-convex cylindrical lens composed of a homogeneous anisotropic material as shown in Fig. 4. As in the case of a single cylindrical interface, we formulate an ODE in the form of $dn/d\theta_k = f(n,\theta_k)$ using the geometric definition of the ideal refraction angles along with anisotropic refraction rules and constrained by Fermat's principle (see the full derivation of the plano-convex lens in Appendix C).

We thus specify the material (Fig. 4(a)) to have the anisotropic refractive index required to attain diffraction limited focusing as shown by the fan diagram in Fig. 4(b), and ray traces (red lines) in Fig. 4(c). The fan diagram shows all rays within the pupil cross the axis within 100nm of the nominal focus, which is well below the diffraction limit. Figure 4(c) also presents the $\hat{k}$-vector directions (blue lines), showing they do not converge to a single point but still generate rays (in red) that do focus within the diffraction limit. Figure 4(d) compares the rays traced for the TRAM design (in red) with the rays traced for an isotropic lens with

Optics EXPRESS

the same geometry (refractive index n = 1.5, in light blue). This shows that, for a given geometry, the optimal material improves the performance over the isotropic case.

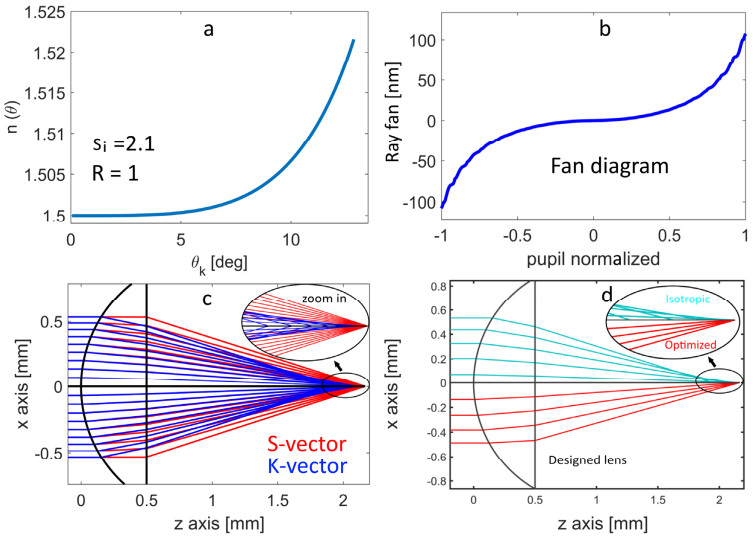

Fig. 4. Focusing for a plano-convex lens with an object on-axis at infinity. (a) Optimal $n(\theta)$; (b) Ray fan diagram showing tight focusing of the TRAM lens; (c) Ray tracing (red) showing ideal focusing for the anisotropic material and $\hat{k}$ -vector directions (blue) for reference. Zoom in on the Ray tracing showed in the top right inset. (d)- Comparison of plano-convex lens with isotropic material (top, light blue) and TRAM (bottom, red) shows enhanced focusing of the TRAM design.

Cylindrical bi-convex lens

The TRAM method can be extended to more general cases, such as a bi-convex lens. Here we also seek an anisotropic refractive index that will perfectly focus an on-axis object at infinity. However, due to more complex ray geometries, an analytic expression for an ODE cannot be attained without approximations. Therefore, we iteratively optimize the index anisotropy while performing anisotropic ray tracing to test its performance, as depicted in Fig. 5.

For a given lens geometry (see Appendix D for bi-convex lens), the iterative process starts with an arbitrary curve $n(\theta)$ that can be parametrized as a polynomial. Then follows anisotropic ray tracing through the lens and calculation of the ray fan at the chosen position. From the ray fan, the maximum spot size is extracted and defined as a cost function for the optimization (other cost functions can be defined as well). The cost function is fed back to iteratively improve the curve $n(\theta)$, namely by adjusting its polynomial coefficients to minimize the spot size. The process continues until a satisfactory solution is found, e.g. spot size below the diffraction limit. Details of the implementation of the optimization process as well as the anisotropic ray tracing are included in Appendix E. The anisotropic properties can also be tailored to off-axis performance for perfect focusing between two off-axis conjugated points.

Optics EXPRESS

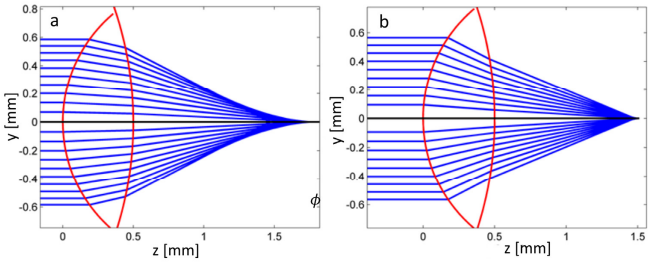

Fig. 5. Enhanced focusing for a cylindrical bi-convex lens with an object on-axis at infinity. (a) Isotropic bi-convex lens; (b) Optimized TRAM lens. The iterative optimization for bi-convex lens is detailed in Appendix E.

4. Physical implementation of TRAM

The design process described above produces an ideal anisotropic material for improved lens performance based on the optimization metric. In this section, we seek to further specify the design based on known electromagnetic properties of anisotropic materials. To determine specific material properties from the refractive index $n(\theta)$, a Fourier transformation from real space to k-space defines the anisotropic homogenous material. We use the dispersion relation $k = \omega n / c$ for monochromatic waves as a scaling factor between *n* and *k*. $n_j = k_j / k_0$, where $k = \omega n / c$. The k-space diagram provides information about the refractive index, phase velocity, and energy of propagating plane waves in a given propagation direction θ. To plot the diagram, we apply a polar-to-Cartesian coordinate transformation:

$$\frac{k_x}{k_0} = n \sin\theta \tag{6}$$

$$\frac{k_z}{k_0} = n \cos\theta$$

The k-space diagrams define the TRAM and an exact realization can be pursued by dispersion engineering of a composite or meta-material [15–17]. Alternatively, it is possible to approximate the TRAM material by uniaxial materials that still preserve the quality of the lens design, for instance including artificial dielectrics [18–21]. The following examples compare the ideal materials to uniaxial birefringent materials, which are described by ellipses in k-space. Figure 6 shows the degree of fit of an ellipse (corresponding to uniaxial materials) to the designed TRAM.

The refractive index plots of Fig. 6(a), 6(c), and 6(e) show that uniaxial birefringent materials are a good approximation for the type of designs presented above. In order to quantify the performance of the perfect focusing lens and uniaxial approximation, we analyze the lens performance for the extraordinary rays of a uniaxial approximation to the ideal design, as depicted in Fig. 6(g). In case of uniaxial materials, the angle between the wave-vector and the Poynting vector is

$$\tan\alpha = \frac{n^2(\theta_k)}{2}\left[\frac{1}{n_e} - \frac{1}{n_o}\right]\sin 2\theta_k \tag{7}$$

Optics EXPRESS

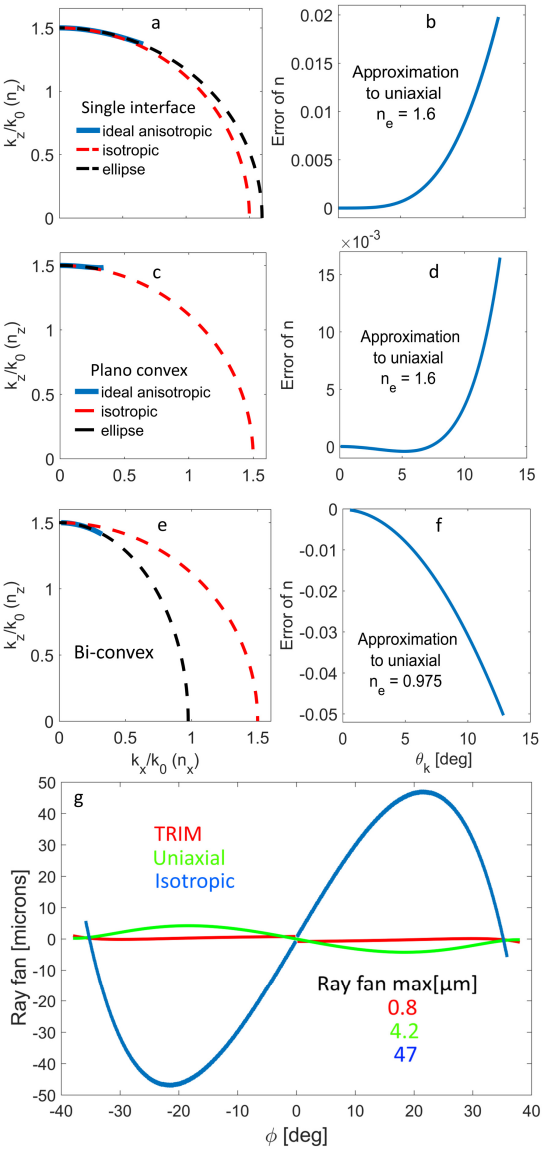

Fig. 6. TRAM approximation and impact on ray fans. (a) k-space diagram for a single cylindrical interface (Blue - optimized refractive index curve. Red - an isotropic reference with $n = 1.5$. Black a fit to uniaxial material with $n_o = 1.5$ and $n_e = 1.6$. (b) Single spherical interface error plot of the difference between the optimized material and uniaxial approximation. (c) k-space diagram for a plano-convex case. (d) Plano convex error plot. (e) k-space diagram for a bi-convex case. (f) Bi-convex error plot (g) Bi-convex ray-fan comparison of TRAM (red), Uniaxial approximation (green), and Isotropic (blue).

As depicted in Fig. 6(g), ray tracing of the approximated uniaxial material in the bi-convex case shows 10x enhancement (evaluated by spot size) over the isotropic material despite the deviation from the ideal design.

5. Discussion

The concept of materials degrees of freedom rather than being originated in materials properties determined a priori (e.g. negative refraction), starts from a systems approach pursuing the ideal material characteristics required to satisfy a given goal. The proposed

Optics EXPRESS

approach, possibly in combination with multi-surface optical design on one hand, and aspheric approaches on the other hand, enables new flexibility at the material level specification facilitating designs with potentially lower complexity (i.e. lower number of elements, lightweight materials, etc). Here, we have left aside macroscopically inhomogeneous materials (GRIN design) and freeform/aspheric optics to be able to evaluate the individual effect of anisotropy as a free design parameter.

The TRAM methodology provides additional degrees of freedom to optimize lenses following specific cost functions as in traditional lens design. In the examples described above we optimized for perfect focusing over a limited field of view, but off-axis performance deteriorates rapidly (see Appendix F). An intrinsic limitation in the field of view stems from the fact that each time a TRAM material is specified for a given ray direction, the ray still undergoes refraction on two surfaces of the lens. Therefore, there are two variables (two refraction angles) to control with only one degree of freedom (refractive index for the given ray direction). As a result, there is a trade-off in performance over the field of view. Optimization of the TRAM lens over a wider field of view, namely compromising the on-axis performance for improved performance over the field of view is also possible, similarly to what is done in traditional lens design (see Appendix G).

The optimal TRAM designs are inherently anisotropic. For linearly polarized light, the ideal designs presented here are valid for cylindrical lenses. In the case of non-polarized light, double refraction occurs, leading to walk-off effects with the improvement, in general, valid for only one polarization state.

Although this report explored TRAM at a functional level, advances in 3D nanofabrication and computational power provide access to these degrees of freedom [22–24]. In particular, direct-write techniques that use ultrashort laser pulses to modify transparent media such as glass [25,26] or polymers [26,27] have been used to create 3D integrated optical devices in bulk material and diffractive optics [25,28,29]. Such techniques in combination with traditional e-beam and multi-layer lithographic approaches could be adapted to scalable fabrication of TRAM adding to the toolbox of lens production approaches.

The TRAM process described above did not consider chromatic dispersion by the material. Furthermore, artificial metamaterials are typically highly dispersive. Hence, the resulting chromatic aberrations will require correction by complementary methods. Still, the 2D (and monochromatic) design is directly applicable to planar systems including photonic integrated circuits.

The extension of TRAM design to 3D elements is beyond the scope of this report. It would be interesting to explore the performance gains arising from the inclusion of an arbitrary anisotropy as a free parameter into the design space. Even though existing optical design software cannot tackle this type of optimization, we expect this report will encourage the development of design tools along these lines. For spherical lenses the optimization is more intricate but still shows promise for improvement over isotropic designs (see Appendix G).

In conclusion, we presented a framework for optical design based on tailoring the materials to optimize a given imaging metric. Within this framework, we implemented Fermat's principle in the design phase and considered the physical realizability via artificial materials. The designed lenses generated perfect imaging even for non-paraxial rays but within a narrow field of view. These simple examples illustrate the best cylindrical (or 2D) lens achievable with a homogeneous (TRAM) material but the extension to use multi-elements, aspherics, and graded index approaches is available to expand the design space.

Appendix A: Ray tracing in anisotropic media

In anisotropic materials, the ray travels in the direction of the pointing vector which is the normal to the gradient of the index surface. The angle $\alpha = \theta_k - \theta_s$ between the $\hat{k}$-vector and the Poynting vector is called the walk off angle. Figure 7(a) depicts the index surface

Optics EXPRESS

description of anisotropic refraction from air into an anisotropic material. The walk off angle is defined as the gradient of the index surface at the point of refraction $\tan\alpha = -dn_z / dn_x$. In polar representation and in small-angle approximation with small $d\theta$ intervals, the walk off angle can be written as $\alpha = \frac{1}{n}\frac{dn}{d\theta}$.

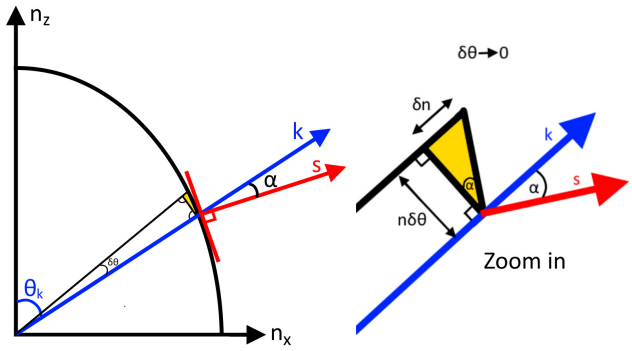

Fig. 7. Diagram for the calculation of rays upon refraction at the interface between isotropic and anisotropic materials. Left- k-space diagram. Right- Zoom in highlighting the definition of the walk-off angle α between the $\hat{k}$ - vector (blue) and the Poynting vector (red).

Based on the index curve $n(\theta_k)$, ray tracing for any imaging geometry can be implemented. The ray tracing procedure is described in this section. The refraction of the extraordinary polarized beam from air into the optimal anisotropic material, follows the generalized Snell law.

$$n_1 \sin\theta_i = n(\theta_2)\sin\theta_2 \tag{8}$$

This equation cannot be solved directly and the solution is obtained from the graphical solution of the k-space diagram, in its numerical version, as depicted in Fig. 8. Accordingly, the transverse conservation of momentum is obtained by calculating the projection of the incident beams and finding its corresponding k-surface refraction numerically.

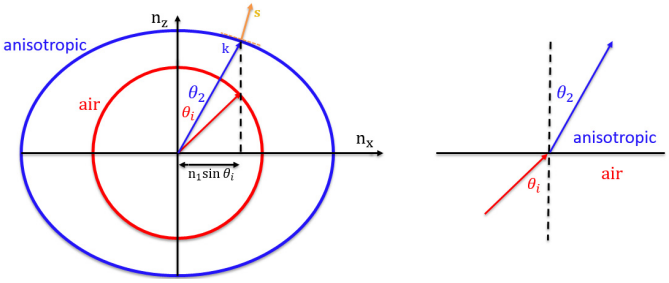

Fig. 8. Principles of anisotropic ray tracing. Left- k-space diagram showing a refraction of a ray traveling from air (red circle) into an anisotropic material (blue ellipse). Conservation of transverse momentum is calculated by projecting the ray onto the x axis, indicating the direction of the $\hat{k}$-vector in the anisotropic material (θ_2). The local surface gradient at the refraction point is calculated, indicating the Poynting vector direction (yellow). Right – real space refraction diagram with corresponding angles.

Unlike a planar interface, at the cylindrical/spherical interface, each ray refraction occurs in a different, tilted, coordinate system, compared to the optical axis, as shown in Fig. 9. Therefore, the anisotropic ray tracing procedure involves rotating the coordinate system for

Optics EXPRESS

each ray according to the geometry of the interface and finding the refraction angles accordingly.

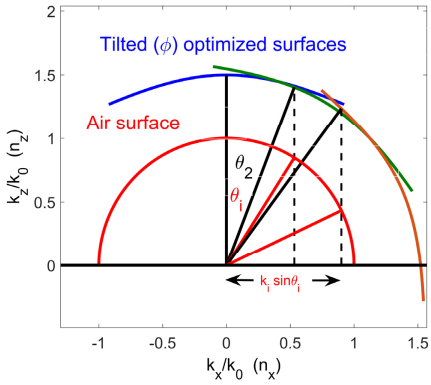

Fig. 9. Numerical solution of the generalized Snell's law in a spherical or cylindrical refractive surface. The anisotropic surface is tilted according to the refraction location at the lens spherical surface. Red, Blue, Green and Orange are examples for tilted anisotropic surfaces. Transverse momentum conservations (Black lines) are illustrated for two arbitrary incident rays (Red lines).

The procedure starts with an optimized $n(\theta)$ curve in Cartesian coordinates $\begin{bmatrix} k_{x1} & k_{x2} \ldots\ldots & k_{xm} \\ k_{z1} & k_{z2} \ldots\ldots & k_{zm} \end{bmatrix}$. For each ray (ϕ), the incident angle is calculated $\theta_i = \phi + \alpha_{beams}$ as well as an appropriate rotation matrix, $R = \begin{bmatrix} \cos\phi & \sin\phi \\ -\sin\phi & \cos\phi \end{bmatrix}$, to adjust the k-surface,

$$\begin{bmatrix} k_{x_{rotated}} \\ k_{y_{rotated}} \end{bmatrix} = \begin{bmatrix} \cos\phi & \sin\phi \\ -\sin\phi & \cos\phi \end{bmatrix} \begin{bmatrix} k_{x_1} & k_{x_2} & \ldots\ldots & k_{x_m} \\ k_{z_1} & k_{z_2} & \ldots\ldots & k_{z_m} \end{bmatrix} \tag{9}$$

where $\begin{bmatrix} k_{x_{rotated}} \\ k_{y_{rotated}} \end{bmatrix}$ is the adjusted k-surface. n_{θ_2} is found graphically by projecting the refraction point ($\hat{k}$-vector at angle θ_t intersects with the adjusted k-surface) on the transverse axis k_x. Then the generalized Snell's law can be applied to find the refraction angle of the $\hat{k}$–vector, $\theta_2 = \sin^{-1}\left(\sin\theta_i / n_{\theta_2}\right)$. We define $\theta_k = \phi - \theta_2$ as the angle from the optical axis and calculate the walk off angle, between phase front and Poynting vector,

$$\alpha = \tan^{-1}\left(\frac{1}{n}\frac{dn}{\theta_k}\right) \tag{10}$$

to finally obtain the direction of the refracted Poynting vector, $\theta_s = \theta_k - \alpha$.

Appendix B: Fermat's principle calculation

As described in Section 2 and shown in Fig. 3(d), rays have to follow Fermat's principle. Hence, we calculate the optical path length (OPL) and optical path difference (OPD) for varying s_i to find a solution that satisfies Fermat's principle. The OPL in anisotropic media is the projection of the phase propagation on the ray path. The OPD between two rays is calculated as

Optics EXPRESS

$$\mathrm{OPD}=\mathrm{OPL}_1 - \mathrm{OPL}_0 \tag{11}$$

where

$$\mathrm{OPL} = l_0 + n l_i \hat{k}\cdot\hat{s} = l_0 + n l_i \cos\alpha \tag{12}$$

The ray path in air, l_0, and ray path in the material, l_i, are defined in Fig. 3(a). The angle α is formed by the $\hat{k}$ and Poynting vectors, and n is the anisotropic index of refraction.

Fermat's principle is imposed by finding the point P where the maximal OPD of all rays crossing P is 0. This stationary point is found over all possible points P' and the corresponding $n(\theta)$ For instance, in Fig. 3(d) the P' is varied along the axis (enough due to symmetry) and P is found at s_i=3.005.

Appendix C: Plano convex cylindrical lens – full derivation

In the plano-convex lens example we seek the anisotropic refractive index of a cylindrical lens that will perfectly focus an on-axis object at infinity. In order to formulate an ODE in the form of $\frac{dn}{d\theta_k} = f(n,\theta_k)$ we define the geometry of the refraction angles and apply the anisotropic refraction rules.

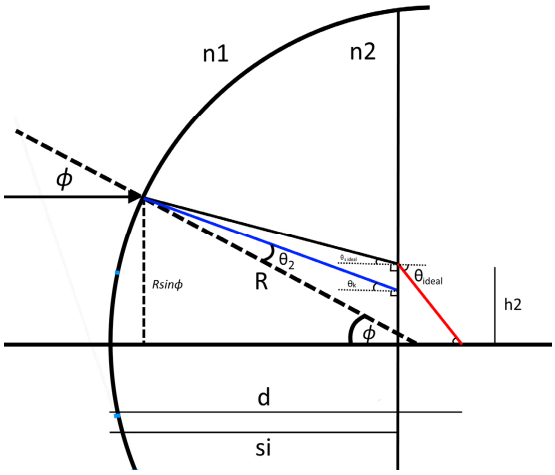

Fig. 10. Plano-convex lens geometry.

We seek again the anisotropic refractive index of a cylindrical lens that will perfectly focus an on-axis object at infinity. This case involves a second refraction at the planar interface as shown in Fig. 11.

$$\theta_{ideal} = \tan^{-1}\left(\frac{h_2}{s_i - d}\right) \tag{13}$$

We also know from conservation of transverse momentum that the second refracted angle is

$$\theta_{ideal} = \sin^{-1}\left(n\sin\theta_k\right) \tag{14}$$

The second refraction height can then be calculated:

$$h_2 = R\sin\phi - \tan\theta_s * \left(d - R + R\cos\phi\right) \tag{15}$$

Combining the two results:

Optics EXPRESS

$$\sin^{-1}\left(n\sin\theta_k\right)=\tan^{-1}\left(\frac{R\sin\phi-\tan\theta_s*\left(d-R+R\cos\phi\right)}{s_i-d}\right) \tag{16}$$

The goal now is to extract θ_s

$$\tan(\sin^{-1}(n\sin\theta_k))=\frac{R\sin\phi-\tan\theta_s*\left(d-R+R\cos\phi\right)}{s_i-d} \tag{17}$$

$$\begin{aligned}\tan(\sin^{-1}(n\sin\theta_k))*(s_i-d)&=R\sin\phi-\tan\theta_s*\left(d-R+R\cos\phi\right)\\ \tan\theta_s*\left(d-R+R\cos\phi\right)&=R\sin\phi-\tan(\sin^{-1}(n\sin\theta_k))*(s_i-d)\end{aligned} \tag{18}$$

$$\theta_s=\tan^{-1}\left(\frac{R\sin\phi-\tan(\sin^{-1}(n\sin\theta_k))*(s_i-d)}{\left(d-R+R\cos\phi\right)}\right) \tag{19}$$

As before in the infinity corrected imaging:

$$\phi=\tan^{-1}\left(\frac{n\sin\theta_k}{n\cos\theta_k-1}\right) \tag{20}$$

Substituting Eq. (27) in to Eq. (26):

$$\theta_s=\tan^{-1}\left(\frac{R\sin\left(\tan^{-1}\left(\frac{n\sin\theta_k}{n\cos\theta_k-1}\right)\right)-\tan(\sin^{-1}(n\sin\theta_k))*(s_i-d)}{\left(d-R+R\cos\left(\tan^{-1}\left(\frac{n\sin\theta_k}{n\cos\theta_k-1}\right)\right)\right)}\right) \tag{21}$$

θ_s can be substituted into the OED

$$\frac{dn}{d\theta_k}=n\tan\left(\theta_k-\theta_{s_{ideal}}\right) \tag{22}$$

Leading to

$$\frac{dn}{d\theta_k}=n\left(\theta_k-\tan^{-1}\left(\frac{R\sin\left(\tan^{-1}\left(\frac{n\sin\theta_k}{n\cos\theta_k-1}\right)\right)-\tan(\sin^{-1}(n\sin\theta_k))*(s_i-d)}{\left(d-R+R\cos\left(\tan^{-1}\left(\frac{n\sin\theta_k}{n\cos\theta_k-1}\right)\right)\right)}\right)\right) \tag{23}$$

Solving this equation provides, in principle, a solution for perfect imaging for every s_i. However, only one of these solutions will satisfy the fundamental Fermat's principle.

We tested the Plano-convex anisotropic design (Sec. 3 and Fig. 4) using our developed ray tracing software. On axis illumination (0°) shows reduction of the Spot RMS size from 20 microns with an isotropic singlet to <400nm using the anisotropic design. At larger fields of view of 4-10°, corresponding to illumination angles of 2-5°, the anisotropic design shows advantages over an isotropic solution. However, as the field of view grows the enhancement is reduced.

Optics EXPRESS

Appendix D: Bi convex cylindrical lens, non-paraxial, ray tracing in anisotropic media

The anisotropic ray tracing described above can be directly applied in any cylindrical geometry. In the case of bi-convex lens, we perform the ray tracing without any approximations in the trigonometric expression by deriving the trigonometric relations needed for the optimization. The basic magnitudes of the non-paraxial ray tracing procedure are shown in Fig. 10.

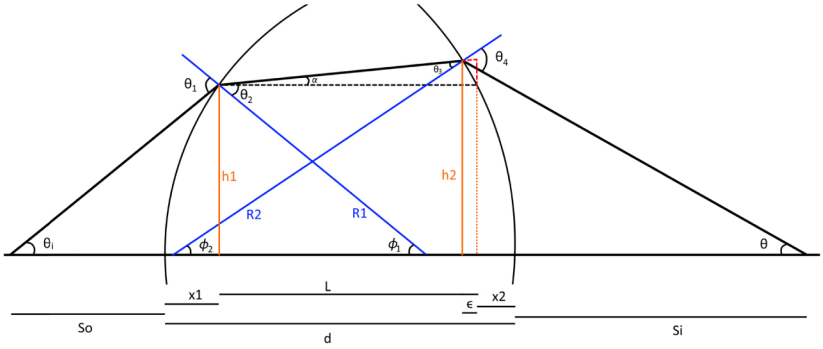

Fig. 11. Geometry of the bi-convex lens. All the angles and dimensions, required for non-paraxial ray tracing, are indicated.

According to the angles and distances, defined in Fig. 10, the trigonometric relations are:

$$h_1 = R_1 \sin\phi_1 \tag{24}$$

$$x_1 = R_1\left[1-\cos\phi_1\right] \tag{25}$$

$$\theta_1 = \phi_1 + \theta_i = \phi_1 + \tan^{-1}\left[\frac{h_1}{s_o + x_1}\right] \tag{26}$$

$$\theta_2 = \sin^{-1}\left[\frac{n_1 \sin}{n_2(\phi_1)}\right] \tag{27}$$

θ_2 is calculated according to anisotropic ray tracing numerical / graphic calculation of appendix A. The ray tracing continues with the following trigonometric relations:

$$\alpha = \theta_2 - \phi_1 \tag{28}$$

$$L = d - (x_1 + x_2) \tag{29}$$

$$x_2 = R_2\left[1-\cos\left(\sin^{-1}\frac{h_1}{R_2}\right)\right] \tag{30}$$

Next, we formulate two equations with two unknown variables, ϵ and h_2;

$$x_2 + \epsilon = R_2\left[1-\cos\left(\sin^{-1}\frac{h_2}{R_2}\right)\right] \tag{31}$$

$$h_2 = (L-\epsilon)\tan\alpha + h_1 \tag{32}$$

Optics EXPRESS

The analytic solution is not straightforward, extracting h_2 involves a numerical solution of the following equation:

$$h_2 - \left(L + x_2 - R_2 \left[1 - \cos\left(\sin^{-1} \frac{h_2}{R_2} \right) \right] \right) \tan\alpha - h_1 = 0 \tag{33}$$

With the exact numerical solution for h_2 we continue to ray trace:

$$\phi_2 = \sin^{-1}\left(\frac{h_2}{R_2} \right) \tag{34}$$

$$\theta_3 = \phi_2 - \alpha \tag{35}$$

$$\theta_4 = \sin^{-1}\left[\frac{\sin\theta_3 \; n_2(\phi_1)}{n_1} \right] \tag{36}$$

The refracted direction is calculated according to the anisotropic ray tracing numerical / graphic solution. Note that there is one angle of propagation in the lens, α, that corresponds to each ray at ϕ_1. The final imaging angle is:

$$\theta = \theta_4 - \phi_2 \tag{37}$$

Using this formalism, all rays can be accurately traced. The optimization procedure, described later, modifies the index curve to improve the lens performance iteratively.

Appendix E: Bi-convex lens - anisotropic index optimization algorithm

In the bi-convex lens we also seek an anisotropic refractive index that will perfectly focus an on-axis object at infinity. Without any approximations in the trigonometric expression we cannot attain an analytic expression for the ODE as in prior cases because the geometry is too complex. However, we can iteratively optimize the index anisotropy as shown below and preform anisotropic ray tracing to test the performance of the design.

The calculation of optimal TRAM material starts with a given radii of curvature of the lens and an arbitrary initial curve $n(\theta)$, parametrized as a polynomial. In this particular case, the initial curve was a solution of a similar plano-convex lens. Then follows an anisotropic ray-tracing through the lens and a calculation of the ray fan at the desired focal length. From the ray fan diagram, we extract the maximum spot size and define it as the cost function. On the following step, the curve $n(\theta)$ is modified by adjusting its polynomial coefficients, and ray-tracing through the lens is performed. The cost function is calculated again and fed back to a minimization algorithm. The optimization algorithm we used is based on golden selection and parabolic interpolation and implemented in MATLAB. The optimization process continues until a satisfactory solution is found such that the polynomial coefficients of the $n(\theta)$ curve generate a ray trace with minimal spot size. Fig. 12 depicts the iterative flow of the ray tracing.

Optics EXPRESS

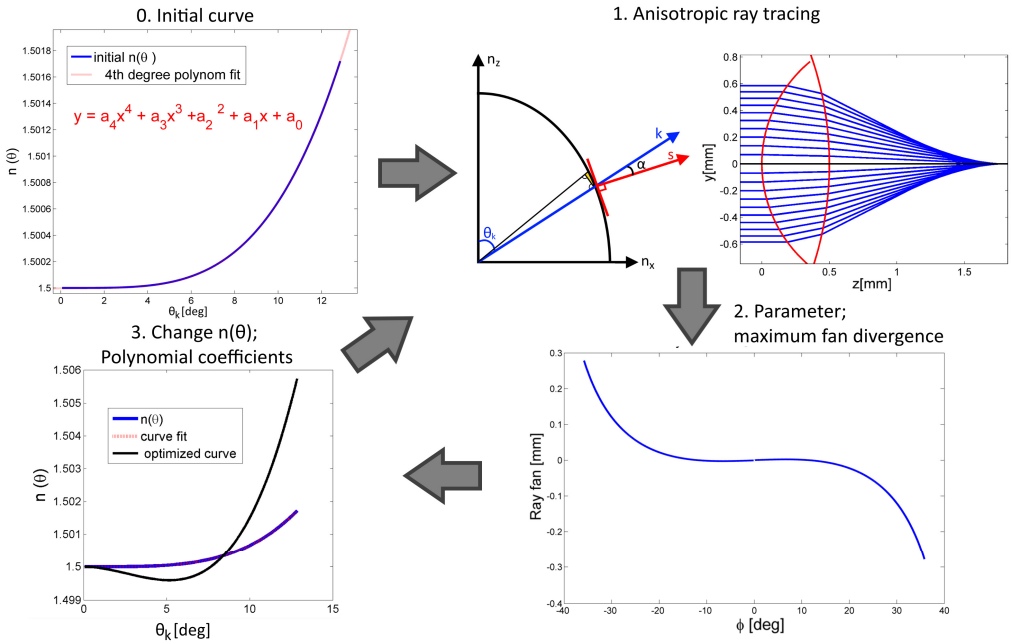

Fig. 12. Iterative optimization of the index $n(\theta)$ for a bi-convex lens. 0. Initial curve $n(\theta)$, parametrized as a polynomial. 1. Anisotropic ray tracing. Principles (left) and biconvex lens example (right). 2. Ray fan diagram. The maximum divergence indicates the spot size, is defined as a cost function, and used as feedback for the minimization algorithm 3. Modification of the curve $n(\theta)$ by changing the polynomial coefficients.

In order to obtain a physically meaningful lens we verify Fermat's principle is satisfied. In the bi-convex case, simulation of the OPD involves several steps of optimization and ray tracing. We optimize the curve $n(\theta)$ and look for a zero OPD point as well as perfect focusing around the paraxial focusing distance of the isotropic lens.

Appendix F: Oblique focusing on single interface

In this section, the performance of a single interface anisotropic lens is compared to isotropic simple lens. The anisotropic material properties were calculated for the case of on axis imaging ($\alpha = 0$) and tested at various angles, $\alpha = 0$, 5, 10, and 20 degrees. The depicted results in Fig. 13 show that the anisotropic material corrects well all the spherical aberration on axis ($\alpha = 0$). However, as the oblique angle grows, aberrations appear. Table 1 compares the ray tracing maximal spot size between the isotropic and the anisotropic lenses at the designed focal plane (3mm). The table shows superior performance of the anisotropic simple lens over isotropic lens at the paraxial focal plane of 3mm. Note that aspheric surfaces would better correct for aberrations in the isotropic case. However, the rationale for comparing spherical surfaces is to understand whether or when anisotropic design can improve performance relative to isotropic design with all other parameters being equal.

Table 1. Comparison of isotropic vs anisotropic oblique focusing in a single interface.

angle	Isotropic spot size [μm]	anisotropic spot size [μm]	Plane location
0	359	2.9	3mm
5	465	173	3mm
10	591	342	3mm
20	902	647	3mm

Optics EXPRESS

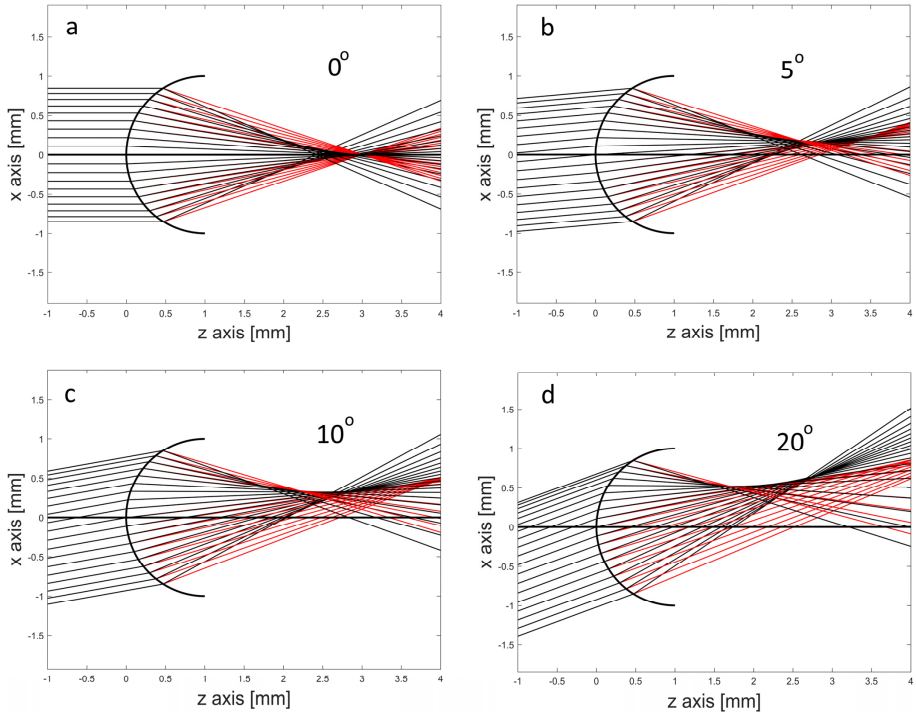

Fig. 13. Oblique focusing on single interface of isotropic (black) vs anisotropic (red) at an angle of (a) 0° (b) 5° (c) 10° and (d) 20°.

Appendix G: Uniaxial spherical lens

In the previous sections, we compared the performance of TRAM to conventional cylindrical lenses for input linear polarization. For spherical lenses, direct semi-analytical calculations to solve the material inverse design are more intricate. However, the observation that anisotropy can help improve performance is still valid and can be used as a free parameter in global optimizations. To illustrate this concept, in Fig. 14 we compare the performance of a spherical lens for isotropic and anisotropic designs using a commercial ray tracing software (Zemax). Because the commercial software cannot include a general material design, we restrict the design to a uniaxial material with c-axis along the lens optical axis and evaluate performance for the extraordinary rays, which in this case correspond to radial polarization. We consider n_o = 2.0 and n_e = 1.5 and an image space F# 1. The performance is tested for input angles of α = 0, 5, 10, and 20 degrees with optimization weights of 1.0, 0.2, 0.1, and 0.05 respectively, to emphasize best on-axis imaging performance. The geometry and the focal plane of the lenses were optimized to minimize the spot radius.

Optics EXPRESS

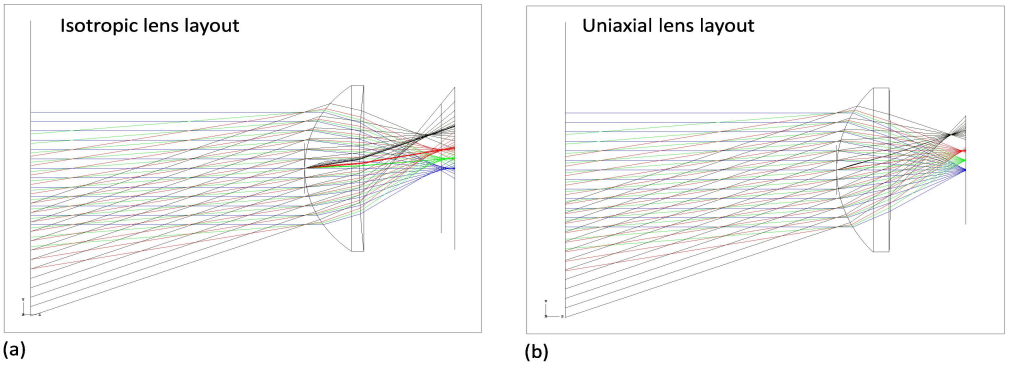

Fig. 14. Oblique focusing through an (a) Isotropic and (b) Uniaxial spherical lens for incident angles of 0°, 5°, 10°, and 20°.

Table 2 compares spot-size performance for both lenses showing better performance for the extraordinary rays in the anisotropic lens. The tangential and sagittal ray fan plots of the two lenses were also compared as shown in Fig. 15. It can be seen that for all field angles, the ray aberration of the uniaxial lens shows superior performance as compared to the isotropic lens.

Table 2. Comparison of r.m.s. spot sizes for isotropic vs uniaxial oblique focusing through a spherical lens.

Angle (°)	Isotropic spot size [μm]	uniaxial spot size [μm]
0	6.71	1.88
5	7.48	1.57
10	11.96	4.94
20	41.27	24.57

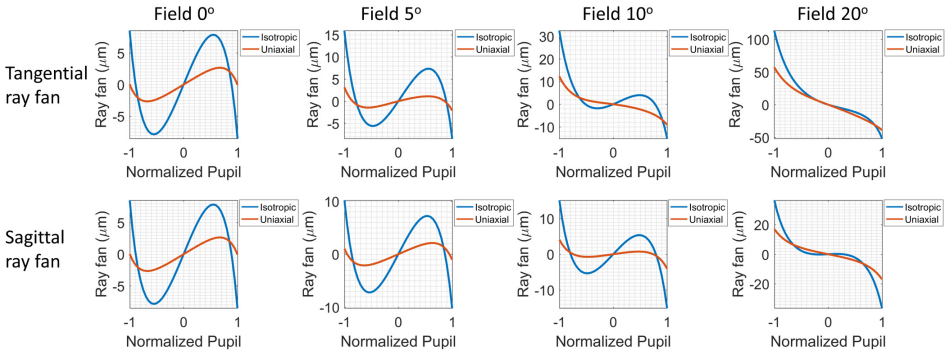

Fig. 15. Tangential (top) and Sagittal (bottom) ray fan comparison between the isotropic (blue) and uniaxial lens(red) for incident angles of 0°, 5°, 10°, and, 20° (left to right).

Funding

DARPA (W911NF12C0044); NSF (1310487).

Acknowledgments

We thank Kenneth Kubala and Adam Greengard for fruitful discussions.